STUDY OF THE CLOSE ENVIRONMENT OF THE ACTIVE NUCLEUS IN NGC 1068 BY DECOMPOSITION OF [O III] AND Hβ EMISSION-LINE PROFILES

DANIELLE ALLOIN AND DIDIER PELAT
Observatoire de Paris-Meudon

ALEC BOKSENBERG
Royal Greenwich Observatory, Herstmonceux Castle

AND

WALLACE L. W. SARGENT
Palomar Observatory, California Institute of Technology
Received 1983 February 25; accepted 1983 May 13

ABSTRACT

We analyze and discuss in this paper the [O III] $\lambda\lambda4959,5007$ and Hβ emission-line profiles observed in various positions over the central region in NGC 1068. The profiles change drastically over a spacing of $1''.2$. We have performed a quantitative decomposition of these profiles using Gaussian individual components and find a clear separation of the following systems:

i) A narrow feature (FWHM ~ 100 km s^{-1}) seen both along position angle PA = 55° and 145°. This component follows the stellar rotation observed in PA = 55°, while it appears to have large radial motions in PA = 145°. It shows up more strongly along PA = 55°, which is also the position of the major axis corresponding to the inner spiral arm structure observed in this galaxy. The value of its line intensity ratio $I([\text{O III}]\ \lambda\lambda4959+5007)/I(\text{H}\beta) = 8$ is compatible with a classical ionization by hot stars, although not uniquely. We interpret this feature as the line emission from ionized regions in the inner disk of the galaxy. Along the minor axis, the overall emission from this component is weaker and corresponds to gas in a lower stage of ionization.

ii) A narrow feature (FWHM ~ 100 km s^{-1}) detected in the NE quadrant. Dynamically this is clearly separated from the disk narrow feature along PA = 55°, while the value here found for the line intensity ratio, $I([\text{O III}])/I(\text{H}\beta) = 17$, implies ionization by nonstellar radiation. We attribute this feature to a nebulosity seen in projection in the NE quadrant, but most probably situated out of the plane of the disk and directly photoionized by the synchrotron emission from the active nucleus in NGC 1068.

iii) A broad (FWHM = 1670 km s^{-1}), blueshifted component ($V_e - V_{\text{systemic}} = -210$ km s^{-1}) is found in both the [O III] and the Hβ line profiles. From the present results this feature seems to be slightly extended (about 240 pc in radius) rather than being confined to the center, suggesting that the broadening is due to a widely distributed collection of cloudlets or filaments and not to an organized motion such as that of a rotating disk, which could not be so large.

iv) A characteristic of the individual clouds detected in the central region of NGC 1068 is that the blueshifted ones are also the more central, as is seen in other objects.

Subject headings: galaxies: individual — galaxies: internal motions — galaxies: nuclei

I. INTRODUCTION

Dynamical and kinematical properties of active galactic nuclei can be derived from the analysis of emission lines profiles in the following ways: (i) by studying the profiles and velocities of a number of emission lines covering a large range in ionization potential (Ward 1978; Pelat, Alloin, and Fosbury 1981): large-scale kinematical properties typically over regions from 0.1 to 100 pc in radius are thus indicated; (ii) in the case of active galactic nuclei for which some spatial resolution can be achieved in the narrow line region (NLR), by analyzing moderate or high-resolution profiles of a few emission lines, obtained at different position angles across the object (Walker 1968a, b; Ulrich 1973; Glaspey et al. 1976; Glaspey, Walker, and Stockton 1976; Pronik 1978; Pelat and Alloin 1980, 1982; Alloin et al. 1981): this allows the detailed study of individual clouds and nebulosities.

The active nucleus of NGC 1068 is a good case for the second approach. The results we present here demonstrate how the profiles of the [O III] $\lambda\lambda4959,5007$ and
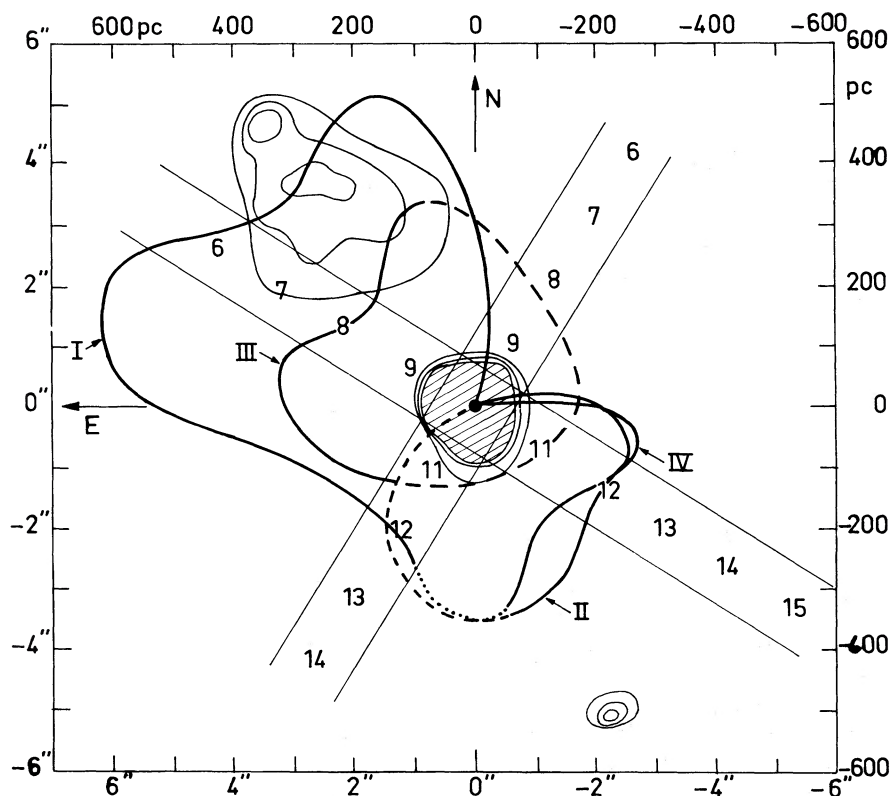
FIG. 1a.—*Thick line*, sketch of the emitting clouds following Walker (1968a). *Thin line*, radio contours at 4885 MHz following Condon *et al.* (1982). Slit positioning of the present IPCS data showing the spatial increment numbers.

Hβ lines vary drastically over regions of 1″ (100 pc[1]). In § II we present our observational data and results of the quantitative line profile decomposition in terms of Gaussian components, in § III we discuss the results, and in § IV we make some concluding remarks regarding (a) the kinematics of the narrow Hβ and [O III] emission lines in a region 12″ in diameter, and its implications, (b) the spatial extent of the broad blueshifted [O III] and Hβ emission, and (c) the spatial location and evolution of the different clouds which show up in the analysis.

II. OBSERVATIONAL DATA AND RESULTS OF THE LINE PROFILE DECOMPOSITIONS

a) Observational Data

The observations (A.B.; W.L.W.S.) were obtained at the coudé focus, equipped with a field rotator, of the Palomar 5 m telescope. The University College London Image Photon Counting System (IPCS) (Boksenberg 1978), mounted at the spectrograph 36 inch (91 cm) camera, was used in 2D mode with a format containing

1000 spectral and 18 spatial increments. The entrance slit was set 1″ wide, and the widths of the contiguous spatial increments detected along the slit were each 1″.2. The comparison arc lines have a measured FWHM of 0.4 Å, and the instrumental profile is closely Gaussian in shape.

We used two slit position angles: PA = 55°, which corresponds to the major axis determined from the set of bright spiral arms just outside the nucleus[2] (Walker 1968a) and PA = 145°, along the minor axis of this system.

Superposed on a sketch of the clouds (following Walker 1968a), we show in Figure 1a the positions at which we obtained line profiles, and in Figure 1b the profiles themselves. More information on our observations is given in Table 1.

b) Wavelength Calibration and Reduction

A linear regression fit was used along each spatial increment to define the wavelength scale from the comparison arc spectra, leading to a precision of about 0.08 Å in the final wavelength calibration process.

---

[1] We assume $H_0 = 50$ km s^{-1} Mpc^{-1} throughout.

[2] The nucleus itself is rather elongated along PA = 30° (1″.2 × 1″.5).

N

E

50

80

100

60

100

200

1000

250

6000

3000

1000

100

150

6000

20

80

60

1.2″

5000   5040 Å
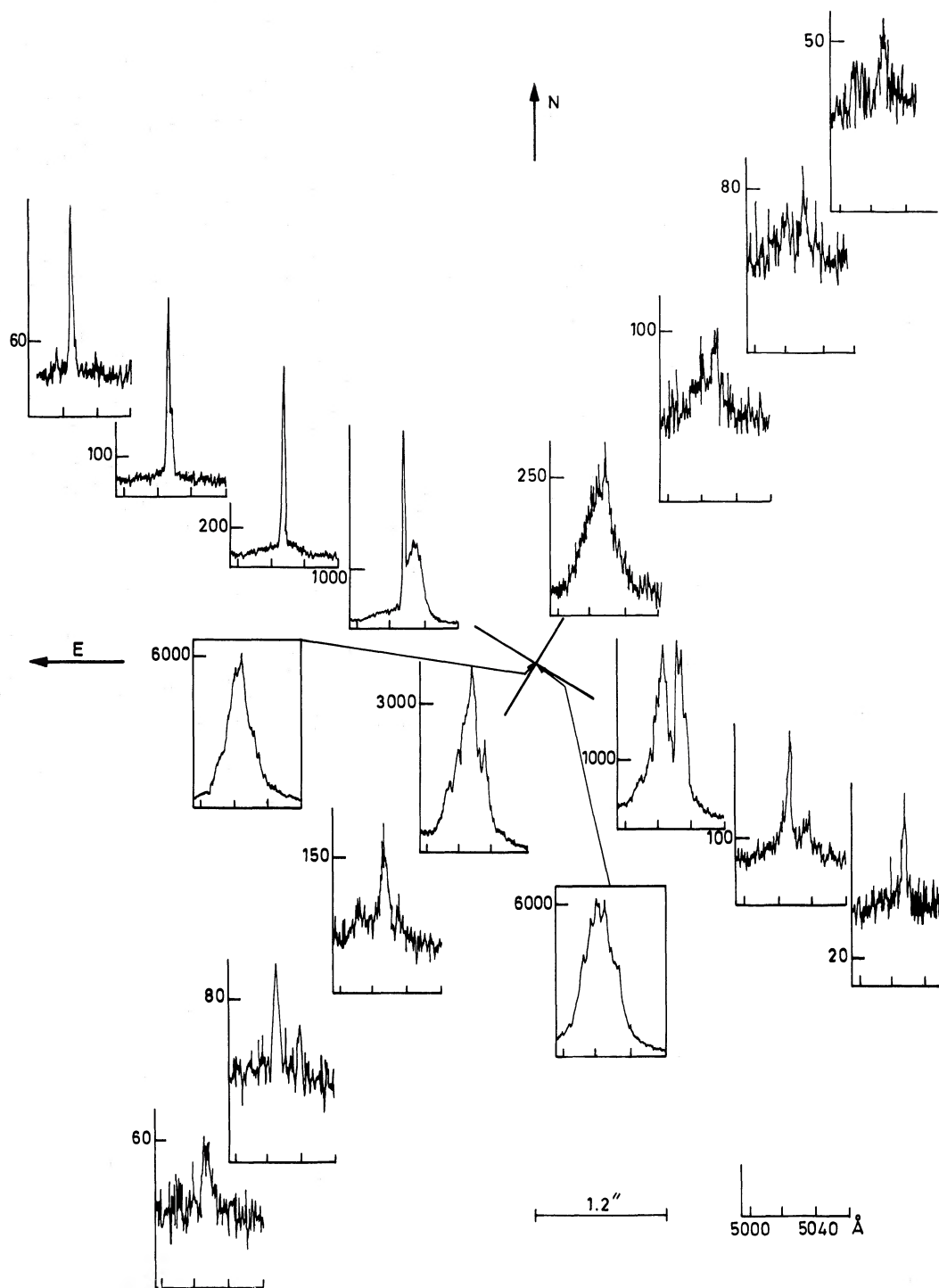
FIG. 1b.—Spatial variation of the [O III] λ5007 line profile along PA = 55° and 145°

OBSERVATIONAL DATA

PA (deg)	Exposure Time (s)	Slit Width (arcsec)	Seeing (arcsec)	1975 November
55	1200	1	<1	10
145	1200	1	<1	10

Regarding the comparison of the Hβ and [O III] line intensities along one particular increment, these data, which were obtained in the youth of the IPCS, were not corrected for image tube S-distortion in the now conventional automatic way before recording. A crude photometric correction was applied to the data by forcing the apparent continuum to have the flat shape it is known to have over the wavelength interval 4861–5020 Å. The mean value of the correction is about 30% on the Hβ intensity relative to [O III], and this mostly gave the correct value of 3 for the [O III] $\lambda\lambda 5007/4959$ line intensity ratio. Nevertheless, due to the need for this correction, the precision in line intensity determination is somewhat uncertain, and the lack of full geometric correction also introduces some uncertainty into the comparison of [O III] and Hβ profiles.

c) Line Profile Decomposition

We used a least-squares fitting routine to analyze and decompose the complex profiles (Pelat and Alloin 1980). This method makes it possible to extract narrow and broad features with a high level of confidence. On the other hand, it has relatively large uncertainty in cases

for which components of about the same width and intensity have to be separated. The resolution of the decomposition process, for a given profile, depends on the signal-to-noise ratio in the original data. In the present study, this ratio varies from one spatial increment to the next and in consequence there is a variation in the number of components to input in the analysis. This introduces a difficulty in following the spatial evolution of a given cloud, unless it clearly stands out in the profile. In illustration of this, we show in Figure 2 a comparison of three different solutions (using Gaussian profiles for the individual components) for the [O III] $\lambda 5007$ line profile analysis relating to the central increment along PA = 55°, indicating how merging of clouds can occur from a difference in the details of the analyzing procedure. For the same data we also did an analysis using Lorentz functions for the shapes of the individual components. Results of the best decomposition then achieved are presented in Table 2 and Figure 3, compared with a decomposition using Gaussian profiles. We never achieved as good a χ^2 using Lorentz functions as for Gaussians. This is due mainly to the difficulty of reproducing the broad feature well with Lorentz functions.

In fact, we do not know whether a "cloud" indeed represents a single, distinct feature or the grouping in space and velocity of a large number of cloudlets which we do not distinguish. If the first, we may expect the emission-line profile to be Gaussian when the cloud is ruled dominantly by macroscopic turbulence, although we are aware of possibly significant departures from this simple shape if some dust is present. If the second, we just assume a Gaussian distribution for the cloudlets,
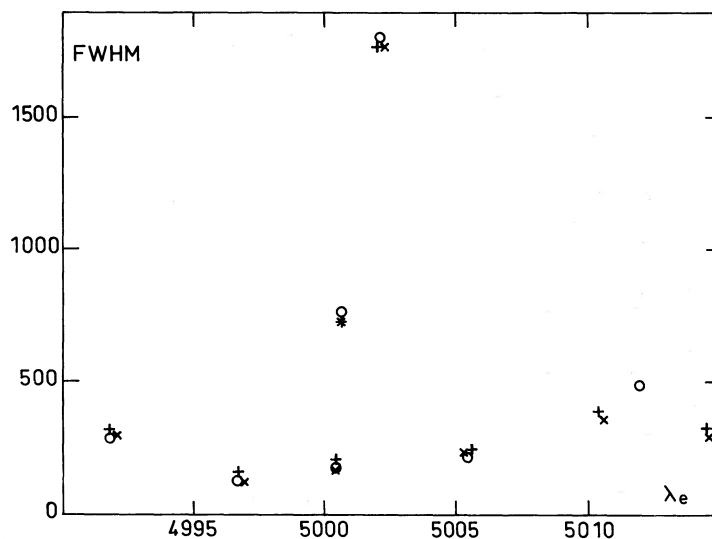
FIG. 2.—Comparison of different decompositions of the [O III] $\lambda 5007$ line profile from the central increment in PA = 55°, in the (FWHM, λ)-plane. *Open circles*, $\chi^2 = 1.8569$. *Plus signs*, $\chi^2 = 1.7476$. *Crosses*, $\chi^2 = 1.7468$.

TABLE 2

LINE PROFILE ANALYSIS FOR THE [O III] λ5007 LINE, CENTRAL INCREMENT IN PA = 55° AND 145°:
COMPARISON WITH DATA FROM PELAT AND ALLOIN (1980)

| PA = 55° | | | | | | PA = 145° | | | | PELAT AND ALLOIN 1980 | | |
| Gaussian Function | | | Lorentz Function | | | Gaussian Function | | | | Gaussian Function | | |
(i)	(ii)	(iii)	(i)	(ii)	(iii)	(i)	(ii)	(iii)	(iv)	(i)	(ii)	(iv)
175	307	34	160	482	121	132	246	11	0.16	207	367	+0.10
466	129	14	467	424	64	...	...	...	...	527	250	+0.32
682	184	28	436	471	91	731	247	28	−0.23	707	150	+0.15
697	734	146	703	329	124	746	670	152	−0.07	...	...	...
795	1778	440	1237	824	110	966	1739	281	−0.10	877	2020	−0.04
985	223	35	991	350	144	969	165	21	0.08	1047	585	[a]
1288	375	42	1321	356	52	1082	364	54	[a]	1147	50	[a]
1524	308	20	1529	398	53	1435	340	32	[a]	1437	84	[a]
										1557	234	[a]

NOTE.—The values given for each component in this table are: (i) V_e, the heliocentric emission velocity (km s^{-1}); (ii) FWHM (km s^{-1}); (iii) the relative intensity of the Gaussian or Lorentz function; (iv) [V_e(PA = 55°) − V_e(PA = 145°)]/⟨FWHM⟩; [V_e(1980) − V_e(1983)/⟨FWHM⟩.

[a]Absence of correspondence.
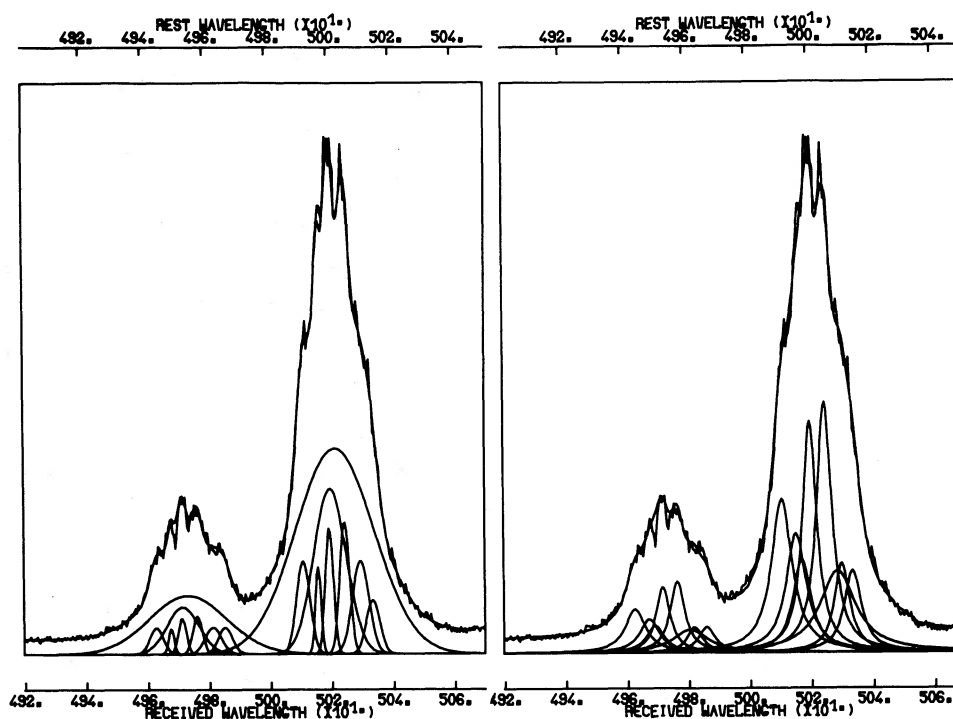
FIG. 3.—Comparison of the decomposition of the [O III] λλ4959, 5007 line profiles (PA = 55°, central increment) using Gaussian (*left*) and Lorentz (*right*) functions for the shape of each individual component.

whatever is the exact line profile for an individual one. For simplicity, in the present study we shall use Gaussian fitting only.

We present in Figures 4a and 4b, respectively, [O III] λ5007 and Hβ line decompositions for several increments near the center in PA = 55°. In Figure 5, we show similar data for the central increments in PA =145°.

Final results of the analysis of the Hβ and [O III] line profiles, using Gaussian individual components are given in Tables 3, 4, 5, and 6.

d) Comparison with Previous Results

We compare the [O III] λ5007 line decomposition from the present data, PA = 55° central increment, to
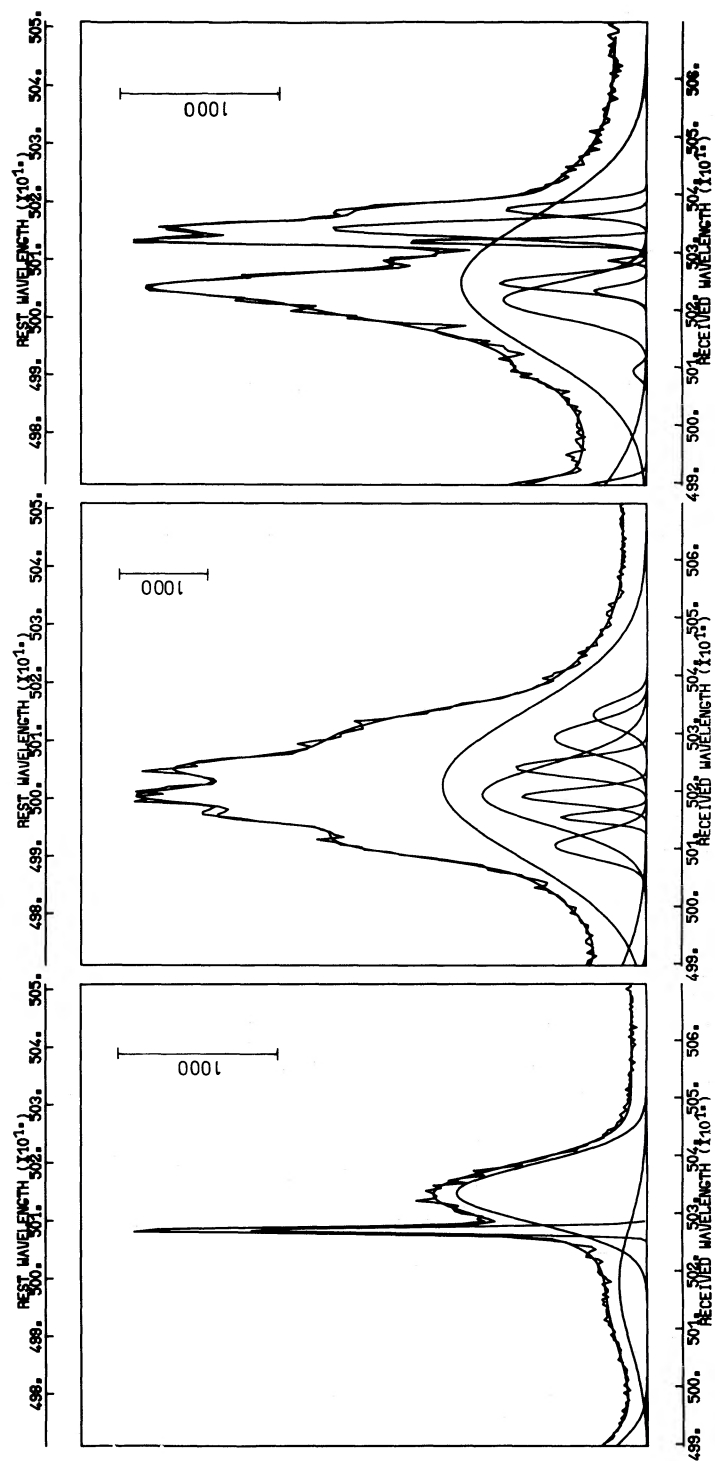
FIG. 4.—(a) Spatial evolution of the [O III] λ5007 line profile and its subsequent decomposition, across the central increments in PA = 55°. From increment 9 (left) to 11 (right). (b) Similarly for the Hβ profile.

498

Fig. 4b

499
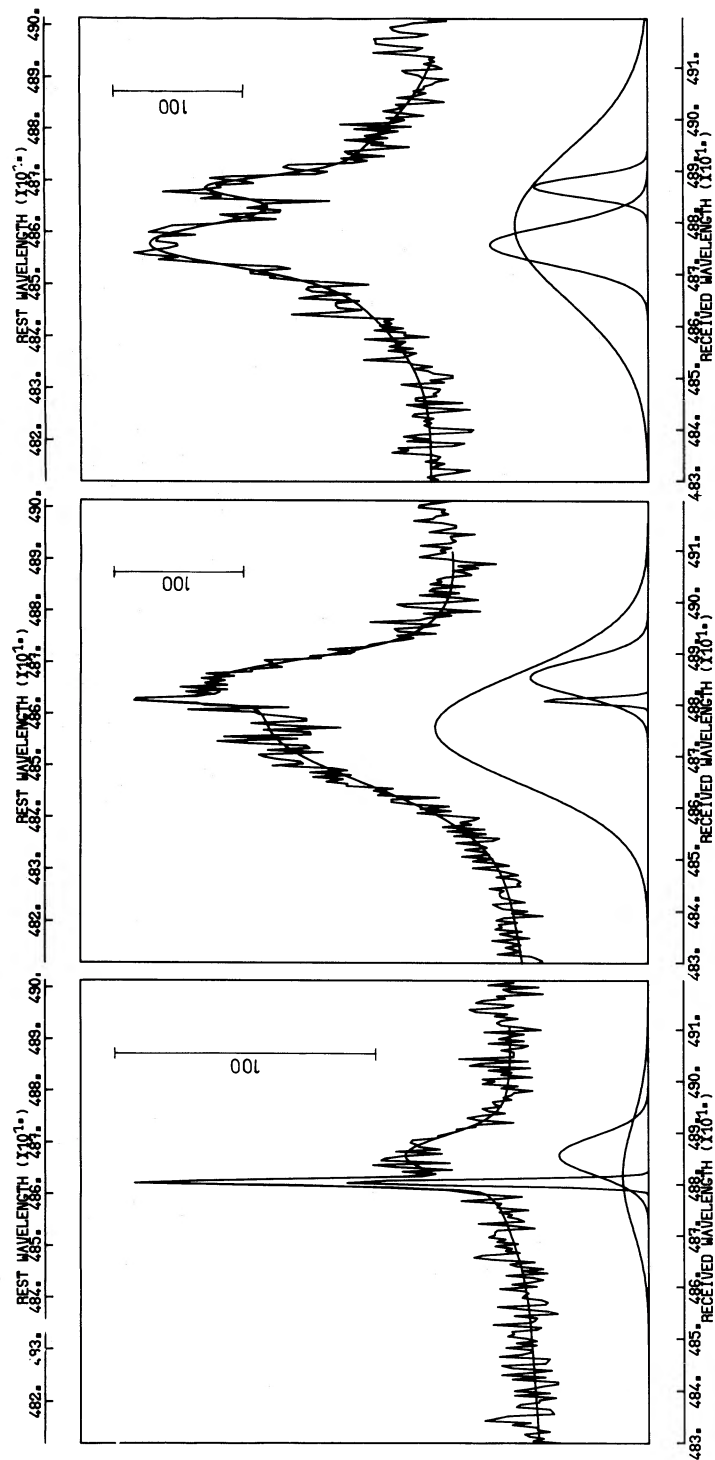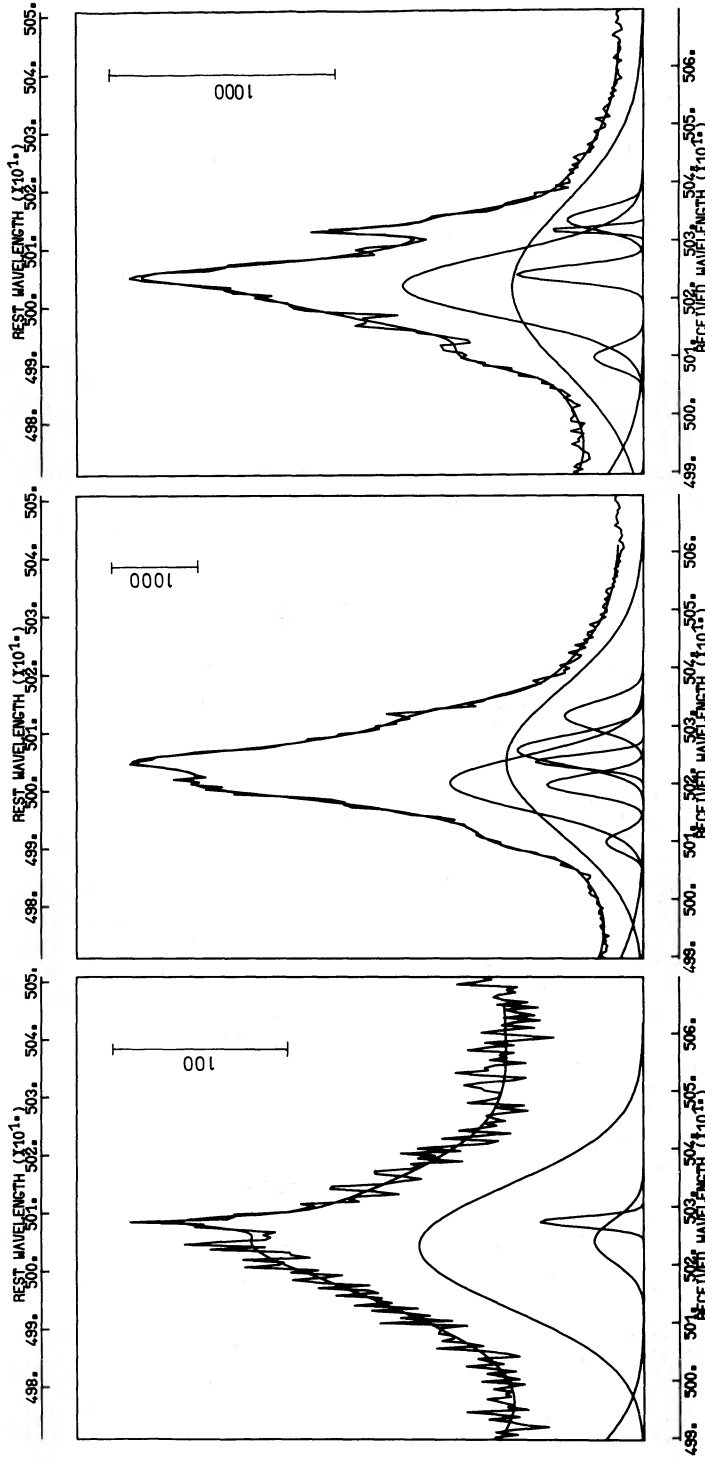
FIG. 5.—Spatial evolution of the [O III] λ5007 line profile and its subsequent decomposition, across the central increments in PA = 145°. From increment 9 (*left*) to 11 (*right*).

TABLE 3
MAJOR AXIS (PA = 55°) ANALYSIS OF [O III] λ5007 PROFILE

Increment Number	r (arcsec)	a	m	l	e	b		k / c+j	j		c		d / d_1	d_2 / d_1+d_2	i
SW															
14	4.8									1115 / 183 / 0.3					
13	3.6									1131 / 127 / 0.8					
12	2.4							989 / 330 / 1.9		1009: / 1633: / 4.1	1111 / 129 / 1.6		1472 / 30 / 0.2	1598[b] / 94 / 0.2	1774[a,b] / 300 / 1.0
11	1.2	97 / 158 / 1.1						841 / 443 / 34	932 / 134 / 3.8	1009 / 1633 / 163	1018 / 200 / 16	1250 / 54 / 1.1	1445[b] / 70 / 10	1577 / 185 / 32	1783[a] / 160 / 12
10	0		175 / 307 / 34	466 / 129 / 14	682 / 184 / 28	697 / 734 / 146	795 / 1778 / 440	985 / 223 / 35					1288 / 375 / 42	1524 / 308 / 20	
9	1.2				596[c] / 1476: / 30								1156 / 71 / 19	1537 / 692 / 87	
8	2.4					699: / 1506: / 4.4							1143 / 106 / 8.3	1304 / 984 / 4.7	
7	3.6									1036 / 71 / 2.6	1131 / 165 / 2.4				
6	4.8									1048 / 125 / 1.5					
NE															

NOTE.—The values given for each component in Tables 3–6 are: *upper row*, heliocentric emission velocity, V_e (km s^{-1}); *middle row*, FWHM (km s^{-1}); *lower row*, relative intensity. A colon (:) indicates doubtful measurement.

[a] Fe II λ5019? But this component is detected also in the [O III] λ4959 line profile.

[b] Three components if solution for increment 11 is input as a first guess. But the signal-to-noise ratio would allow us to say only that there is a blend at V_e = 1714 km s^{-1}, FWHM = 450 km s^{-1}, and relative intensity 1.4.

[c] The analysis both of the [O III] and Hβ lines along increment 9 leads to a broad, quite blueshifted component which is obviously a *blend* of the broad component found along increment 10 and which, we think, is related to the very central source, and individual clouds also seen in the blue wing. Therefore this blueshifted, large component cannot be compared with the components in the increment 10 decomposition.

the results obtained by Pelat and Alloin (1980) with a better spectral resolution but very little spatial resolution (Table 2). The blue side of the profile is rather similar in the two sets of data: within a precision in $\delta\lambda$/FWHM of 4%–30%, the same clouds are found in both independent analyses. On the other hand, some of the redward clouds, as well as the flare in PA = 30°, appear to be absent in the present data. In fact, in Pelat and Alloin (1980) the slit was larger (2″.3) and swept a sector of 75° centered on PA = 55°; consequently, they included more clouds than in the present observations.

Nevertheless, these new observations imply that the blueshifted clouds which are common to the two sets of data are spatially confined to the very central region, less than 1″ in diameter.

e) Internal Consistency

Another test is to compare the [O III] λ5007 line profiles corresponding to the central increments of the two sets of spectra in PA = 55° and 145° (Table 2). Again, within a precision of 7%–25%, the blue sides of the profiles lead to a similar set of clouds, while the red

TABLE 4

MAJOR AXIS (PA = 55°) ANALYSIS OF Hβ PROFILE

Increment Number	r (arcsec)	k			
SW					
14	4.8		{ 1137 53		
13	3.6		{ 1122 75 0.15		
12	2.4	{ 1047[a] 214 0.5			
11	1.2	{ k 872 563 6.1	1105 2069 19	$d_1 + d_2$ 1565 282 2.2	
10	0	{ 862 1549 51	1190 79 1.4	$d + d_1 + d_2$ 1465 498 9.0	
9	1.2		1160 86 1.8	$d + d_1 + d_2$ 1488 544 3.2	
8	2.4		1130 142 0.7		
7	3.6	{ 1055 39 0.3	1153 79 0.15		
6	4.8	{ 1060 174 0.3			
NE					

[a] May be two components with the narrower of FWHM ~ 100 km s^{-1}, at 1078 km s^{-1}.
For explanation of rows, see notes to Table 3.

sides are slightly more discrepant (see Figs. 4*a* and 5). Nevertheless, this once more suggests that the blueshifted emitting clouds are more confined to the center than the redshifted ones. Apart from the emission velocities and widths of the components, their relative contributions to the energy in the line do not appear identical in the two profiles. The broad component, in particular, apparently contributes more to the line profile in the spectrum obtained in PA = 55°, where it is also seen with a larger blueshift. All this can be explained in terms of centering and guiding uncertainties, with the central region in NGC 1068 being not absolutely quasi-stellar.

III. DISCUSSION

a) The Narrow Components

Narrow components are found both in the [O III] and Hβ line profile analyses. We detect them to a distance

up to 5″ from the center along both directions PA = 55° and 145°.

i) Major Axis

Comparing the velocity measurements for the Hα and [N II] emission lines by Burbidge, Burbidge, and Prendergast (1959) obtained at PA = 55° with the results of Duflot (1963) and Walker (1968*a*) (after constructing an interpolation between the velocity curves at PA = 41° and 71°) shows the former to be systematically larger: at r = 10″ from the center the discrepancy reaches 60 and 80 km s^{-1} in the SW and NE quadrants, respectively.

In Table 7A we list the characteristics of the narrow features found in the decompositions of the different profiles along PA = 55°, both in the Hβ and [O III] λ5007 lines, and give corresponding intensity ratios. In Figure 6 a plot of these results is shown with data for

TABLE 5
Minor Axis (PA = 145°) Analysis of [O III] λ5007 Profile

Increment Number	r (arcsec)													
SE														
15	6											1099		
												194		
												0.25: [a]		
14	4.8											1055[b]		
												274		
												0.83[c]		
13	3.6											1062		
												200		
												0.9		
		a?												
12	2.4	208			853							1142		1644
		157			1598							243		98
		0.3			4.4							1.7		0.3
		a			b + c								d	f
11[d]	1.2	127			847	874			988				1440	1548
		261			2001	765			194				73	259
		9.5			192	235			18				5.2	14
		a	e	b						c			d	
10	0	132	731	746				966	969	1082			1435	
		246	247	670				1739	165	364			340	
		11	28	152				281	21	54			32	
									b + c					
9	1.2					922	946:		982		1179			
						1474	30:		523		127			
						19	0.2		1.5		0.8			
			e											
8	2.4		772			871:						1234		
			197			1557:						175		
			0.2			4.0						0.6		
			g											
7	3.6		643									1275		1678
			304									249		148
			0.5									0.7		0.3
6	4.8											1190		
												358		
NW												0.6		

[a] Uncertainty ~ 50%.
[b] Probably two components.
[c] Uncertainty ~ 30%.
[d] The [O III] 5007/4959 lines cannot be brought back to a ratio of 3 when correcting for a flat continuum.

the gaseous component, from Walker's measurements on [O II], Hγ, Hδ, and [Ne III] in PA = 41° and 71°. Clearly, two different systems appear:

i) One which we call the disk component, more or less follows the rotational motion of the stellar component (see Walker's 1968a results). This component is seen, both in Hβ and [O III] line emission, on increments 13, 12, (SW quadrant), and 7 and 6 (NE quadrant). The corresponding line ratio has a mean value $I([O\ III]\ \lambda\lambda 4959 + 5007)/I(H\beta) = 8 \pm 3$, while the relative intensity of the [O III] line emission from this feature de-creases regularly outward. From the line intensity ratio $I([O\ III])/I(H\beta)$, we might expect such a feature to be identified with rather classical H II regions. On the other hand, the regular spatial decrease of its intensity argues against this: at a resolution of 100 pc, a group of distinct H II regions would produce a patchy intensity distribution along the slit, which is not observed.

ii) Another component, appearing on increments 9, 8, and 7 (NE quadrant), does not follow the rotational disk pattern. This feature is already visible in Walker's measurements of the gaseous component in PA = 41°, al-

TABLE 6
Minor Axis (PA = 145°) Analysis of Hβ Profile

Increment Number	r (arcsec)	a	b+c			d+f
SE						
14	4.8				1027	
					106	
					0.3[a]	
13	3.6				1022	
					138	
					0.6	
12	2.4				1089	
					283	
					1.0	
		a	**b+c**			**d+f**
11	1.2	135	863	984	1069	1496
		343	709	2119	264	325
		1.1	12	15	2.0	2.7
			b+c			**d**
10	0	822	880	959		1452
		30	531	1624		183
		0.3	7.4	30		1.0
9	1.2				1253	
					112	
					0.5	
8	2.4				1251	
					112	
					0.45	
7	3.6				1252	
					65	
					1.15	
6	4.8				1250	
					79	
					0.7	
NW						

[a] Uncertainty ~ 30%.

though no comment about it was made at that time. A simple explanation would be that this component is not coplanar with the disk. Its mean line ratio $I([\text{O III}])/I(\text{H}\beta) = 17 \pm 3$ is significantly larger than the one encountered in the disk component. From this line ratio, the FWHM of this feature (about 100 km s^{-1}), and its probable separation from the disk, we conclude that it represents a nebulosity of low electron density ionized by the central nonstellar source, of the kind found in NGC 3516 (Ulrich and Péquignot 1980).

ii) Minor Axis

The characteristics of the narrow features appearing in the decomposition of the [O III] and Hβ profiles along this direction are listed in Table 7B and compared with the velocities of the gaseous component measured by Walker (1968a) in PA = 130° and 160° (see Fig. 7). Significant radial motions appear around those direc-

tions in the SE quadrant: this is discussed thoroughly by Walker (1968a). More particularly, the gaseous and stellar components do not show similar behavior in the SE quadrant for PA = 160° and the NW quadrant for PA = 130°. The line intensity ratio $I([\text{O III}])/I(\text{H}\beta) \approx 2$, on the other hand, is still lower than in the disk component found along PA = 55°, and may depend on the relative exposure to the nonstellar ionizing radiation from the active nucleus. Indeed, the absolute line fluxes are decreasing rapidly outward, being about 3 times smaller along PA = 145° than along PA = 55°. Thus, we note that the narrow component system is weaker and corresponds to a lower excitation along PA = 145° than PA = 55°. The relative decrease is still steeper in the NW quadrant than in the SE: this might result from a slight shift in centering of the object. However, the central increments both in PA = 55° and 145° show the same absolute line flux, which indicates that the centering in fact was rather good in both directions. Another

TABLE 7A

NARROW COMPONENTS, PA = 55°

Increment Number	r (arcsec)	[O III] λ5007		Hβ		$I([O\ III])/I(H\beta)$		Relative $I([O\ III])$	
		Disk	Neb.	Disk	Neb.	Disk	Neb.	Disk	Neb.
SW									
14	4.8	1115 183		1137 53				0.3	
13	3.6	1131 127		1122 75		7		0.8	
12	2.4	1111 129		1078[a] 100		4–8		1.6	
11	1.2	1018 200	1250 54					16	1.1
10[b]	0	985 223			1190 79			35	
9	1.2		1156 71		1160 86		14		19
8	2.4		1143 106		1130 142		16		8.3
7	3.6	1036 71	1131 165	1055 39	1153 79	11	21	2.6	2.4
6	4.8	1048 125		1060 174		7		1.5	
NE									

NOTE.—The values given for each component in Tables 7A and 7B are: *Upper row*, heliocentric emission velocity, V_e (km s^{-1}). *Lower row*, FWHM (km s^{-1}).

[a] May be two components with the narrower of FWHM ~100 km s^{-1}, at 1078 km s^{-1}.

[b] The [O III] line profile in the center is obviously dominated by highly ionized material and by the blueshifted filaments. It explains the difference between the Hβ and [O III] line profiles.

possible explanation would be the presence of dust in the NW quadrant.

b) The Broad Component

Within the framework of our analysis, using Gaussian components, we find evidence for a broad, blueshifted feature in the center of NGC 1068, extending at least 240 pc in diameter. Relative to its central intensity, it is present along PA = 55° at a level of respectively 1%, 7%, 37%, and 1% for increments 8, 9, 11, and 12, and along PA = 145° at a level of respectively 1.5%, 7%, 68%, and 1.6% for increments 8, 9, 11, and 12. To check the reality of this broad feature beyond the central increment (remembering that a "point" image may straddle two spatial increments) we have computed the expected spread in energy resulting from atmospheric smearing with a seeing value of 1″ (see Appendix). For seeing < 1″, consistent with our observations, the contribution to the observed levels in the extended broad component are negligible. This is borne out by the abruptness with which the observed line profiles change between increments (Fig. 1b).

If, indeed, the broad component is not confined to the center, it would suggest that its larger width is due to the contribution of numerous clouds; otherwise, a huge organized structure, more than 100–200 pc in radius, should be present.

Right in the center, on increment 10, the broad component represents respectively 58% and 50% of the global [O III] line emission for the data obtained along PA = 55° and 145°, respectively. The value of the line ratio $I([O\ III])/I(H\beta)$ for the broad component alone is around 12. This value appears to be slightly smaller than the one obtained for the entire profile, about 17±4, more typical of a Seyfert 2 galaxy. Therefore the broad component tends to show up characteristics rather of the narrow line region in a Seyfert 1.5. Considering the bulk of the [O III] line emission (over a region 120 pc in radius) in the broad feature alone, with an electron density of 10^5 cm^{-3} (Walsh 1983) and electron temperatures of 10^4 K and 1.5×10^4 K, we find oxygen abundances of, respectively, 4.7×10^{-4} and 1.11×10^{-4}, assuming that all the oxygen in this zone is in the form O^{++}.

Owing to the large FWHM of the broad component, its emission velocity is less precisely determined than in the case of narrow features: an uncertainty of up to ±100 km s^{-1} might be expected. Considering the re-

TABLE 7B

NARROW COMPONENTS, PA = 145°

Increment Number	r (arcsec)	[O III] λ5007		Hβ		I([O III])/(Hβ)		Relative I([O III])	
SE									
15	6.0	1099 194						0.25	
14	4.8	1055 274		1027 106		< 3		0.83	
13	3.6	1062 200		1022 138		2		0.90	
12	2.4	1142 243		1089 280		2.2		1.7	
11	1.2	988 194	1440 73[a]	1069 264	1496 325[a]	12	2.6	18	5.2
10	0	969 165	1435 340[a]		1452 183[a]			21	32
9	1.2	946 30	1179 127	1253 112		2.1		0.8	
8	2.4	1234 175		1251 112		1.8		0.6	
7	3.6	1275 249		1252 65		0.8		0.7	
6	4.8	1190 358		1250 79		1.1		0.6	
NW									

[a] This component rather corresponds to the edge of a cloud seen on increment 10 at 1435 km s^{-1} with a FWHM of 340 km s^{-1}.

sults from the Hβ and [O III] line profiles in PA = 55° and 145°, a mean set of parameters for the broad feature is the following: heliocentric emission velocity 895 km s^{-1}; FWHM 1670 km s^{-1}. These values are in reasonable agreement with those found by Pelat and Alloin (1980) from their [O III] line profile analysis, respectively 877 km s^{-1} and 2020 km s^{-1}. The difference in the FWHM of the broad feature probably results from a slightly different assumed setting of the underlying continuum. However, the present results confirm the blueshift of the broad feature, both in the [O III] and in the Hβ line, by about 210 km s^{-1}.

c) Spatial Evolution of the Discrete Clouds

We attempt to summarize, in Tables 3 to 6, the information we have derived from the line decomposition, on discrete clouds. Some clouds can be recognized and followed spatially. Thus, in the SE quadrant, cloud (a) extends up to 2″4 from the center. Clouds (b) and (c), which represent an important fraction of the [O III] line emission in its blue wing, are confined to the central increments and are seen both in PA = 145° and 55°. Clouds (g) and (e) on increments 7 and 8 in the NW quadrant, also on the blue side of the line, might represent an extension of clouds (e) and (b), though the velocities differ by about 100 km s^{-1}: if so, this velocity difference would represent the velocity range within this particular cloud. In the red wing, at PA = 145°, cloud (d) is clearly outlined, extending to the SE up to 1″2. For the set of data along PA = 55°, we find a complex of clouds extending up to 2″4 on the SW, with redshifted emission velocities up to +700 km s^{-1}. To the SW again, another cloud, (k), can be separated. Other features can be recognized, but, as we discussed previously, the difference in signal-to-noise ratio from one increment to the next limits the degree of decomposition we can achieve: clouds cannot be deblended when going outside the central increments, therefore it is difficult to follow all of them spatially.

The clouds we find in correspondence with Walker's (1968a) conclusions are as follows: $(d_1 + d_2)$ correspond roughly to cloud I, (i) to cloud II, (k) to cloud IV, while cloud III, which in his study extends up to about 2″5 from the center, seems on the contrary to be rather well confined to the central increment in our data.

In Figure 1a, which represents the contours of forbidden-line clouds as sketched by Walker, we have repro-
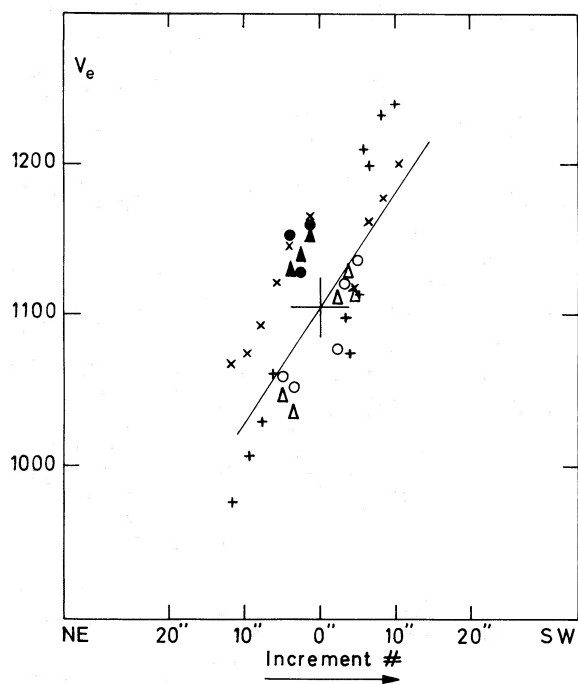
FIG. 6
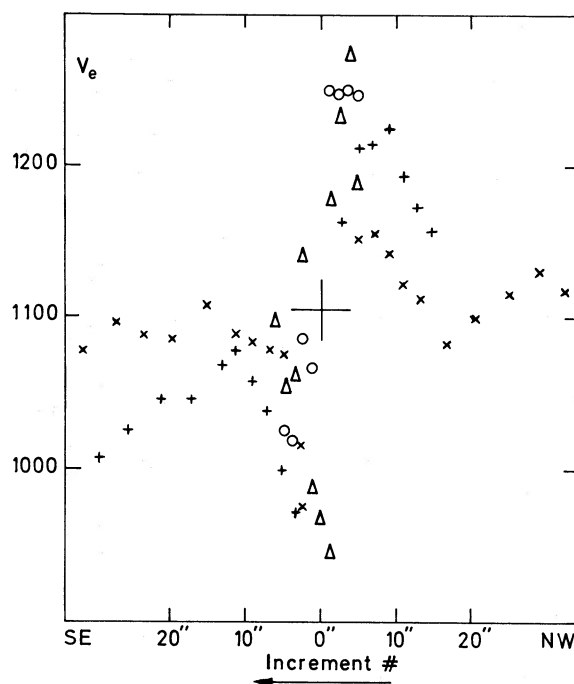
FIG. 7

FIG. 6.—Heliocentric velocity of the narrow Hβ and [O III] emission lines as a function of the increment position, in PA = 55° ($V_{systemic}$ = 1107 km s^{-1}). Triangles refer to the [O III] λ5007 line. Circles refer to the Hβ line. Open symbols correspond to the disk component (I([O III])/I(Hβ) ~ 8). Filled symbols correspond to the nebular component (I([O III])/I(Hβ) ~ 17). Crosses indicate the gaseous component seen by Walker (1968a) in PA = 41°. Plus signs indicate the gaseous component seen by Walker (1968a) in PA = 71°. The continuous line indicates the stellar disc in PA = 55° interpolated from Walker's measurements in PA = 41° and 71°.

FIG. 7.—Heliocentric velocity of the narrow Hβ and [O III] emission lines as a function of the increment position, in PA = 145° ($V_{systemic}$ = 1107 km s^{-1}). Triangles refer to the [O III] λ5007 line. Circles refer to the Hβ line. Crosses indicate the gaseous component seen by Walker (1968a) in PA = 160°. Plus signs indicate the gaseous component seen by Walker (1968a) in PA = 130°.

duced the radio contours from VLA map at 4885 MHz (Condon et al. 1982). The two outermost radio components show an elongation along roughly the same PA as do the [O III] line emission contours, but the radio emission cannot be said to follow closely the forbidden-line region: apart from the NE extended radio component which coincides more or less with part of cloud d_2 (I in Walker's sketch), all the other clouds have no radio counterpart at this level of flux detection. Most of the radio emission at 4885 MHz comes from the central core, less than 1″ (100 pc) in diameter. Also, at 2.26 μm, the nuclear emission in NGC 1068 is dominated by a core which is found from speckle interferometry to be less than 0″.2 (20 pc) in diameter (McCarthy et al. 1982). The second outer radio component seen in the SW quadrant most probably corresponds to the star cluster seen by Bertola (1966) in PA = 210° at about 5″ from the center.

IV. CONCLUDING REMARKS

The present analysis confirms the presence of a broad, blueshifted component, both in the [O III] and Hβ

emission lines. We find its FWHM to be around 1700 km s^{-1} and its emission velocity 895 km s^{-1}, in reasonable agreement with previous estimates. The line ratio I([O III])/I(Hβ) in this component is about 12. Obviously, it would be necessary to study the profiles of other emission lines such as [Ne V], [O II], [Ne III], and [O III] λ4363 to be able to deduce astrophysical parameters in this zone. But, if we consider this limited result in the context of the relation between the electron density and the FWHM deduced for the Seyfert nucleus in NGC 3783 (Pelat, Alloin, and Fosbury 1981), we can conclude that the broad line component comes from a rather dense region. Assuming n_e = 10^5 cm^{-3} (Walsh 1983) and T_e = 10^4 K leads to an oxygen relative abundance of 4.7×10^{-4}, quite similar to the solar value; this indicates that the ionized gas has been processed normally and enriched through star formation, and is not recently accreted intergalactic gas. There are indications that the broad component is extended.

Regarding the cloud system, the main result of this study is the following: the blueshifted clouds which constitute the blue side of the [O III] line profile are also the innermost ones; again, a similar effect of an increas-

ing emission-line blueshift with a decreasing distance to the central ionizing source has previously been inferred in the narrow line region in NGC 3783 (Pelat, Alloin, and Fosbury 1981). Apart from this, knowledge of the spatial distribution of the discrete clouds which extend up to a few arc seconds from the center is not augmented much by the present work: first, we have data along only two position angles; second, the variation of the signal-to-noise ratio from one increment to the next limits the quality of the line profile fits so that in outer regions spatial adjacent clouds become detected as a blend. Nevertheless, we see the same clouds as outlined in the sketch by Walker (1968a). When compared with VLA radio continuum map at 4885 MHz, we do not see a close relation between the [O III] line emission and the radio emission. This leaves open the interpretation of the relation observed between the total forbidden line and radio power in a number of Seyfert nuclei (de Bruyn and Wilson 1978; Wilson 1979). Instead of applying to the whole of the forbidden line and radio emissive regions, this relation might hold only for the very central source, which emits half of the [O III] line and a large fraction of the radio flux at 4885 MHz (Condon et al. 1982). A higher spatial resolution in both the radio and forbidden-line emission observations should give some clues on this question.

The narrow features appearing in the decomposition of the [O III] and Hβ line profiles can be broadly separated into a disk component, probably representing matter along the line of sight and still close to the active nucleus, and a component which probably originates in a diffuse nebulosity of the kind seen in NGC 3516 (Ulrich and Péquignot 1980). In the latter, from the narrowness of the [O III] and Hβ lines, we expect the electron density to be rather low compared with the value in the broad component or even in the individual clouds. The observed $I([O~III])/I(H\beta)$ line ratio is of the order of that detected in the nebulosity in NGC 3516. At a distance of about 400 pc from the center, we see only the disk component, so this nebulosity—along PA = 55°, in the NE quadrant—does not extend very far. Data along adjacent position angles would help define the angular extent of this nebulosity.

With such a dramatic change in line profile as seen between increments 1″.2, the present results will be greatly improved by the use of the Space Telescope. At the same time, we would like to make the following cautionary remark: in the case of rather close objects like NGC 1068—in which 1″ corresponds roughly to 10^2 pc—spatial variations of the line profile can mimic apparent temporal variations if the observational procedure is not strictly the same for all observations in a given sequence. This effect is relevant for the "narrow" part of the emission (forbidden or permitted). On the other hand, temporal variations of the broad (FWHM a few 10^4 km s^{-1}) permitted features, like the ones detected in NGC 3516, for example (Collin-Souffrin, Alloin, and Andrillat 1973; Boksenberg and Netzer 1977), cannot be affected by the spatial structure of the outer regions, since the emissive source is really confined to a region less than 1 pc across.

APPENDIX

We compute in this appendix the expected spread in energy resulting from atmospheric smearing, considering a seeing of 1″.

The geometric configuration of the problem is shown in Figure 8, the IPCS increments, 1″×1″.2, corresponding to number 10 in the center and then increasing to 11 and 12 along the slit.
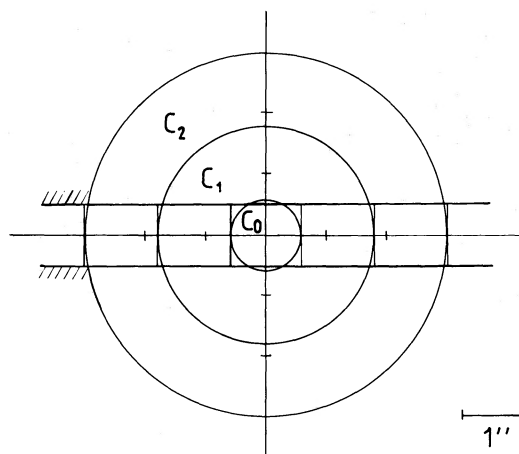
FIG. 8.—Observational geometry: the 1″ slit is represented here horizontally, and divided into five 1″×1″.2 spatial increments. These increments are I_{10} in the center, I_{11} and I_{12} to the right, I_9 and I_8 to the left. A FWHM =1″ star is schematically shown as three circular isophotes of radii 0″.6, 1″.8, and 3″.

1. *Theoretical approach.* If $F_p(r)$ is the point spread function, we normalize it, $2\pi \int_0^\infty F_p(r)r\,dr = 1$, and we shall consider two cases:

a: A Gaussian point spread function:

$$F_p(r) = \frac{\omega_c^2}{4\pi} \exp\left(-\omega_c^2 r^2/4\right),$$

where ω_c is the frequency for which the modulation transfer function (MTF) is attenuated to 0.368.

The following parameters are frequently used:

$$\sigma = 2^{1/2}/\omega_c \approx 1.41/\omega_c, \qquad \mathrm{FWHM} = \sigma \times 2(2\log_e 2)^{1/2} \approx 2.35\,\sigma = 4(\log_e 2)^{1/2}/\omega_c \approx 3.33\,\omega_c.$$

b: The point spread function from the so-called "seeing" theory (King 1971; Johnson 1973). In that case, the point spread function has no analytical form while the MTF, $T(\omega)$, does, and we have

$$F_p(r) = \frac{1}{2\pi} \int_0^\infty J_0(\omega r) T(\omega)\omega\,d\omega, \qquad T(\omega) = \exp\left(-\omega/\omega_c\right)^{5/3},$$

J_0 being the zero order Bessel function.

2. *Numerical application.* With a seeing value $\mathrm{FWHM} = 1''$, $\sigma \approx 0''.425$, $\omega_c \approx 3.33$ arcsec^{-1}, and limits for the integration within rings 1 and 2 are the following:

$$0''.6 \approx 2/\omega_c, \qquad 1''.8 \approx 6/\omega_c, \qquad 3''.0 \approx 10/\omega_c.$$

a: Computation in the case of a Gaussian point spread function. The energy emitted respectively, in the center,

$$C_0 = \frac{1}{\sigma^2} \int_0^{0.6} r \exp\left(-r^2/2\sigma^2\right) dr,$$

in ring 1 (integration limits $0''.6$–$1''.8$) and in ring 2 (integration limits $1''.8$–$3''$), are:

$$C_0 = 0.631, \qquad C_1 = 0.368, \qquad C_2 = 1.3 \times 10^{-4}.$$

We also compute the corresponding energy in the IPCS increments 10, 11, and 12 which is:

$$I_{10} = 0.641, \qquad I_{11} = 0.060, \qquad I_{12} = 8.6 \times 10^{-6},$$

b: Computation in the case of the "seeing" theory. We use numerical values for the point spread function as given by Johnson (1973), to derive the energies C_0', C_1', C_2' corresponding to the center, ring 1, and ring 2.

In fact, we are essentially interested in the comparison of the energy falling into increment 10 to the one into increment 12 since we know that a "point" image may straddle two spatial increments. We will use the approximation:

$$I_{12}' = \left[\frac{1 \times 1.2}{\pi(3^2 - 1.8^2)}\right] C_2' = 0.0663 C_2'.$$

We have computed the integrals for C_0', C_1', and C_2' using the Simpson method:

$$C_0' = 0.632, \qquad C_1' = 0.348, \qquad C_2' = 0.018.^3$$

---

[3] Adopting the "seeing" theory profile does not greatly change the computed energy spread in the center and even in ring 1, but in ring 2 there is a factor of 100 difference. This means that assuming a Gaussian profile for a star image underestimates very much the atmospheric spread far from the center while it is a very good approximation in the center itself.

The comparison of the energies C_0 and C_0' allows us to consider $I_{10}' = I_{10} = 0.641$, while we have

$$I_{12}' = 0.0663 \times C_2' = 0.00119,$$

and finally

$$I_{12}'/I_{10}' = 0.2\%.$$

REFERENCES

Alloin, D., Laques, P., Pelat, D., Despiau, R. 1981, *Astr. Ap. Suppl.*, **43**, 231.
Bertola, F. 1966, *Pub. Obs. Padova*, No. 134.
Boksenberg, A., and Netzer, H. 1977, *Ap. J.*, **212**, 37.
Boksenberg, A. 1978, *Optical Telescope of the Future*, *Conference Proceedings* 1977 Dec. (Geneva: ESO CERN).
Burbidge, E. M., Burbidge, G. R., and Prendergast, K. H. 1959, *Ap. J.*, **130**, 26.
Collin-Souffrin, S., Alloin, D., and Andrillat, Y. 1973, *Astr. Ap.*, **22**, 343.
Condon, J. J., Condon, M. A., Gisler, G., and Puschell, J. P. 1982, *Ap. J.*, **252**, 102.
de Bruyn, A. G., and Wilson, A. S. 1978, *Astr. Ap.*, **64**, 433.
Duflot, R. 1963, *J. d'Obs.*, **48**, 247.
Glaspey, J. W., Eilek, J. A., Fahlman, G. C., and Auman, J. R. 1976, *Ap. J.*, **203**, 335.
Glaspey, J. W., Walker, G. A. H., and Stockton, A. 1976, *Ap. J.*, **210**, 27.
Johnson, C. B. 1973, *Appl. Optics*, **12**, 1031.
King, I. 1971, *Pub. A.S.P.*, **83**, 199.
McCarthy, D. W., Low, F. J., Kleinmann, S. G., and Gillett, F. C. 1982, *Ap. J. (Letters)*, **257**, L7.
Pelat, D., and Alloin, D. 1980, *Astr. Ap.*, **81**, 172.
_____. 1982, *Astr. Ap.*, **105**, 335.
Pelat, D., Alloin, D., and Fosbury, R. A. E. 1981, *M.N.R.A.S.*, **195**, 787.
Pronik, V. I. 1978, *Izv. Krym. Ap. Obs.*, **58**, 104.
Ulrich, M. H. 1973, *Ap. J.*, **181**, 51.
Ulrich, M. H., and Péquignot, D. 1980, *Ap. J.*, **238**, 45.
Walker, M. F. 1968a, *Ap. J.*, **151**, 71.
_____. 1968b, *A.J.*, **73**, 854.
Walsh, J. R. 1983, *Astr. Ap.*, in press.
Ward, M. J. 1978, Ph.D. thesis, University of Sussex.
Wilson, A.S. 1979, *Proc. Roy. Soc. London A*, **366**, 461.
Wilson, A. S., and Willis, A. G. 1980, *Ap. J.*, **240**, 429.

D. ALLOIN and D. PELAT: Observatoire de Paris-Meudon, Meudon Principal Cedex-F-92195, France

A. BOKSENBERG: Royal Greenwich Observatory, Herstmonceux Castle, Hailsham, East Sussex BN 27 1RP, England

W. L. W. SARGENT: Department of Astronomy 105-24, California Institute of Technology, Pasadena, CA 91125